Simulation of delamination by means of cohesive elements using an explicit finite element code

E.V. González[1], P. Maimí[1], A. Turon[1], P.P. Camanho[2] and J. Renart[1]

Abstract: This paper presents the formulation of a tri-dimensional cohesive element implemented in a user-written material subroutine for explicit finite element analysis. The cohesive element simulates the onset and propagation of the delamination in advanced composite materials. The delamination model is formulated by using a rigorous thermodynamic framework which takes into account the changes of mixed-mode loading conditions. The model is validated by comparing the finite element predictions with experimental data obtained in interlaminar fracture tests under quasi-static loading conditions.

Keywords: cohesive element, explicit finite element analysis, delamination.

1   Introduction

The application of polymer-based composite materials reinforced with continuum fibres is in gradual expansion as a result of their good specific mechanical properties. However, the application of composites is still limited due to the shortcomings in the models used to predict structural failure. In addition, the absence of reliable strength prediction methods means that the certification process of aeronautical composite structures is based on a time consuming and expensive sequence of physical tests, from coupon to full-component level. To increase the reliability and to reduce the number of tests requested to certify composite structures, efficient design tools validated by means of experimental data are needed. Virtual testing platforms can be an efficient tool to replace some of these mechanical tests (National Research Council of the National Academies (2006)).

Delamination is one of the most common failure mechanisms in laminated composite materials and can appear at any life time of the structure (manufacturing, transportation, assembly, and service). Delamination reduces seriously the integrity of a

---

[1] AMADE, Escola Politècnica Superior, Universitat de Girona, Girona, Spain.
[2] DEMEGI, Faculdade de Engenharia, Universidade do Porto, Porto, Portugal.

structural element and can produce its collapse. Therefore, accurate analysis tools for the simulation of delamination are required.

Delamination has been largely studied and modelled in the literature. When material nonlinearities can be neglected and an initial crack is present, methods based on Linear Elastic Fracture Mechanics have been proven to be effective in predicting delamination growth, such as the virtual crack closure technique (Irwin (1957); Rybicki and Kanninen (1977); Raju (1987); Zou et al. (2001); Krueger (2002)), the J-integral method (Rice (1968)), the virtual crack extension (Hellen (1975)), and the stiffness derivative (Parks (1974)). These techniques are used to calculate the components of the energy release rate. Delamination growth is predicted when a combination of the components of the energy release rate is equal to, or greater than, a critical value (Griffith (1921)).

When no initial macroscopic defects are present, a local approach has been frequently used to detect delamination onset, in which the key parameters are critical values of tractions (e.g. Pagano and Pipes (1973) and Hashin (1980)).

Another approach for delamination modelling can be developed within the framework of Damage Mechanics. Models formulated using Damage Mechanics considers an interface as a third independent material defined by its own constitutive law. This interface links the two structural components and is based on the concept of the cohesive crack model introduced by Barenblatt (1962), Dugdale (1960), Hillerborg et al. (1976) and others: a cohesive damage zone or softening plasticity is developed near the crack front. Cohesive damage zone models relate tractions to displacement jumps at an interface where a crack may occur. Damage initiation is related to the interfacial strength (i.e. the maximum traction on the traction-displacement jump relation). When the area under the traction-displacement jump relation is equal to the fracture toughness, the traction is reduced to zero and new crack surfaces are formed. The use of cohesive models is extremely powerful for the simulation of general fracture processes due to its simplicity and the unification of crack initiation and growth within one model.

The implementation of cohesive constitutive models normally is carried out by means of user-written subroutines in finite element codes. Generally, the examples presented in the literature implement cohesive elements (e.g. Schellekens and de Borst (1993), Allix et al. (1995), Mi et al. (1998), Alfano and Crisfield (2001), Camanho et al. (2003) and De Borst et al. (2006)) or a user material definition (e.g. Pinho et al. (2006), Iannucci (2006) and Aymerich et al. (2008)), although surface-based cohesive behaviours which eliminate the need to define cohesive elements have been also implemented (e.g. Zhang et al. (2006) and Abaqus 6.8 (2008)).

In cases where crack path is known in advance, either from experimental evidence,

or because of the material configuration, discrete interface elements equipped with a cohesive constitutive relation are inserted a priori in the finite element mesh (e.g. Corigliano and Allix (2000)). To allow for a more arbitrary direction of crack propagation, interface elements can be inserted between all continuum elements (Xu and Needleman (1994)). However, this approach is limited to a number of pre-defined orientation crack angles since the interface elements are aligned with the element boundaries. Some authors (e.g. Martha et al. (1993) and De Borst (2003)) use meshing tools to redefine the position of cohesive elements in function of the stress state evolution. When the position for the appearance and progression of a crack is detected, the structure is again meshed and an interface element is located in a proper position. Alternatively, another research line in fracture modelling is to improve the kinematic description of finite elements by enriching the shape functions by means of adding degrees of freedom. Initially, these models consider a law which relates the stresses and the strains until damage localization is detected in one plane. At this point, the law is rewritten and relates stresses and crack opening. Some of these approaches are: elements with embedded discontinuities (e.g. Oliver (2000)) based on the enhanced assumed strain (Simo and Rifai (1990)), and extended finite elements (e.g. Belytschko et al. (2001)) based on partition of unity method (Babuska and Melenk (1997)).

In the formulation of cohesive models, the energy dissipated during the crack opening has to be controlled, i.e. it is necessary to assure that the model satisfies the Clausius-Duhem inequality (Turon et al. (2006)). Some models are well suited to simulate delamination under constant mixed-mode conditions, such as Mi et al. (1998), Alfano and Crisfield (2001). However, these models do not satisfy the Clausius-Duhem inequality when the crack grows in variable mixed-mode conditions, because generally they define the damage threshold parameter as the maximum displacement and the damage variable as a function of material parameters that depend on the mixed-mode ratio. Some examples of cohesive models which develop in a thermodynamically consistent way are Ortiz and Pandolfi (1999), and Jansson and Larsson (2003).

In previous work of the authors, a thermodynamically consistent damage model has been proposed for the simulation of progressive delamination in composite materials under variable mixed-mode ratio (Turon et al. (2006)). The constitutive law follows a bilinear relationship between relative displacements and tractions at the interface, and it is defined by using a delamination onset and propagation criteria. The delamination onset criterion is based on energy terms and is proposed so the model formulation accounts for loading mode changes in a consistent thermodynamically way. The formulation also accounts for crack closure effects to avoid interfacial penetration of two adjacent layers. This model is implemented by using

a user element subroutine, called UEL, where it is defined the zero-thickness cohesive element for implicit analysis in Abaqus finite element software (Abaqus 6.8 (2008)).

Some structural problems cannot be solved by using an implicit finite element code due to convergence difficulties related to material softening. To avoid these difficulties an explicit code should be used. An implicit analysis requires the assembly of the global stiffness matrix and its subsequent inversion to solve the equilibrium equations system for each iteration, whereas with an explicit analysis these operations are not necessary. Explicit integration schemes do not require the solution of a global set of equilibrium equations as the accelerations, velocities and displacements are calculated explicitly at each node recurring to a simple central differences rule applied over a time increment. Consequently, the explicit formulation is often proper in cases where severe changes in stiffness matrix occur, such as analysis with failure or degradation of the material. Other applications where explicit code is recommended and implicit analysis may lead to severe convergence difficulties are problems with complex contacts, post-buckling, and high-speed dynamic events such as impact. Explicit codes can also be used to solve problems that are essentially static by controlling some simulation variables, such as the kinetic energy that must be less than 5% of the internal energy of the system (Abaqus 6.8 (2008)).

In this paper, a modified formulation and implementation in an explicit finite element code of the cohesive model originally developed by Turon et al. (2006) are presented. The model is implemented by using a user-written material subroutine, called VUMAT (Abaqus 6.8 (2008)). The user material developed is defined on sets of elements that represent the possible location for delamination. The elements can be selected to have zero-thickness (surface elements) or non-zero-thickness (continuum elements). The possibility of using continuum-based cohesive elements enables the simulation of an interface with non negligible thickness. Therefore, the macroscopic properties of the interface material, such as stiffness and strength, can be measured experimentally and used directly in the cohesive model.

In the literature, there are also available cohesive models implemented in a user-written material subroutine for explicit finite element analysis. Generally, these models are checked by simulating quasi-static standard delamination toughness tests, and a simulation of delamination in a monolithic composite laminated plate subjected to low-velocity impact is presented as the most challenging application. Under impact loading, delamination growth develops under variable mixed-mode conditions, and this phenomenon must be accounted properly in the cohesive model. However, the formulations available in the literature often do not control the crack growth in a consistent thermodynamically way (e.g. Pinho et al. (2006)).

The contents of this paper are structured as follows: first, the updated formula-

tion of the cohesive model given by Turon et al. (2006) is presented. Next, the adaptations of the formulation to be implemented in a continuum interface are described. After, the implementation of the model in a user-written material is also explained in detail. Finally, the numerical predictions of interlaminar fracture tests of polymer-based composite materials are compared with experimental data in order to validate the model.

2   Damage Model Formulation

The main aspects of the delamination model presented by Turon et al. (2006) are presented in this section with some modifications of the original formulation.

The constitutive law used is shown in Fig. 1. This law is a bilinear relationship between relative displacements and tractions. The first line represents an elastic relationship, prior to damage onset. Damage onset is related with the interface strength τ^o. When the area under the traction-displacement relation is equal to the fracture toughness, G_c, the interface tractions revert to zero and a new crack surface is created.
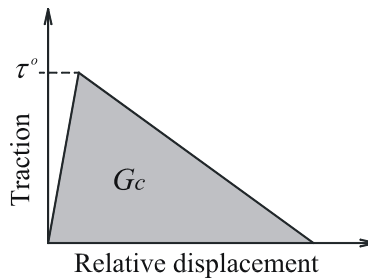

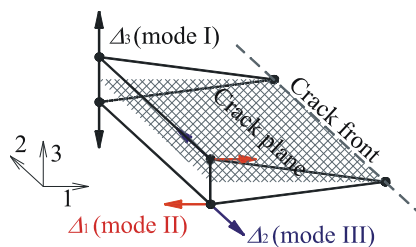Figure 1: Bilinear constitutive law.

Figure 2: Propagation modes.

The different relative displacements between the nodes of a surface element are shown in Fig. 2, where each displacement is directly associated with the corresponding propagation mode by assuming that the crack front is located at the indicated line. At finite element scale level, it is not possible to distinguish the shear modes II and III because the crack front is in fact unknown. For this reason, shear modes are generally grouped together in the formulation of the cohesive models (see section 2.1).

The damage model follows the general formulation of continuum damage models proposed by Mazars (1982), and Simo and Ju (1987). The Helmholtz free energy by unit surface of the interface under isothermal conditions is defined as:

$$\psi(\mathbf{\Delta}_i, d) = (1 - d)\,\psi^0(\mathbf{\Delta}_i) \quad i = 1, 2, 3 \tag{1}$$

where d is the scalar isotropic damage variable and $\psi^0(\mathbf{\Delta}_i)$ is a function of the relative displacement space defined as:

$$\psi^0(\mathbf{\Delta}_i) = \frac{1}{2}\mathbf{\Delta}_i D^0_{ij}\mathbf{\Delta}_j \quad i, j = 1, 2, 3 \tag{2}$$

Eq. 1 indicates that the relative displacement components, $\mathbf{\Delta}_i$, are the free variables of the system (i.e. displacement driven formulation), and d is the internal variable that ensures the irreversibility of the model.

Negative values of $\mathbf{\Delta}_3$ (mode I) have no physical sense because the cracks are closed and no damage is produced. Therefore, the damage model has a unilateral behaviour for this propagation mode, which means that the damage variable can be activated or deactivated as a function of the loading state. Therefore, Eq. 1 is modified as:

$$\psi(\mathbf{\Delta}_i, d) = (1 - d)\,\psi^0(\mathbf{\Delta}_i) - d\psi^0(\delta_{3i}\langle -\mathbf{\Delta}_3\rangle) \quad i = 1, 2, 3 \tag{3}$$

where $\langle - \rangle$ is the Macaulay brackets defined as $\langle x \rangle = \frac{1}{2}(x + |x|)$, and δ_{ij} is the Kronecker delta.

Applying Coleman's method (Simo and Ju (1987)), the constitutive equation reads:

$$\tau_i = \frac{\partial\psi}{\partial\mathbf{\Delta}_i} = (1 - d)D^0_{ij}\mathbf{\Delta}_j - dD^0_{ij}\delta_{3j}\langle -\mathbf{\Delta}_3\rangle \quad i, j = 1, 2, 3 \tag{4}$$

D^0_{ij} is the undamaged stiffness tensor, defined as:

$$D^0_{ij} = \delta_{ij}K \quad i, j = 1, 2, 3 \tag{5}$$

where K is a scalar parameter corresponding to the slope of the first line in the constitutive law, typically called penalty stiffness. As Eq. 5 shows, the penalty stiffness is the same for any propagation mode.

To ensure the thermodynamic consistency of the model, the dissipated energy by surface unit during the damage propagation process, Ξ, has to be equal or greater than zero:

$$\Xi = Y\dot{d} \geq 0 \tag{6}$$

where the thermodynamic force Y associated with the internal variable d is defined as:

$$Y = -\frac{\partial \psi}{\partial d} \tag{7}$$

The value of the damage variable has to be evaluated at each time increment during the loading process. Therefore, it is necessary to define a suitable norm of the relative displacement vector, the surface for damage activation, a law for damage evolution, and criteria for damage onset and damage propagation.

2.1 Norm of the relative displacement vector

The selected norm of the relative displacement components is defined as:

$$\lambda = \sqrt{\langle \mathbf{\Delta}_3 \rangle^2 + \mathbf{\Delta}_{shear}^2} \tag{8}$$

where $\mathbf{\Delta}_3$ is the relative displacement in mode I, and $\mathbf{\Delta}_{shear}$ is the Euclidian norm of the relative displacements in mode II and mode III:

$$\mathbf{\Delta}_{shear} = \sqrt{\mathbf{\Delta}_1^2 + \mathbf{\Delta}_2^2} \tag{9}$$

Normally, the shear modes II and III are represented together because their individual evaluation depends on the relative displacement between homologous nodes with respect to the crack front orientation. Since at finite element scale level the crack orientation is generally unknown, it is not possible to distinguish between modes II and III.

2.2 Surface of damage activation and law for damage evolution

The surface of damage activation from Turon et al. (2006) is modified by the expression:

$$F(\mathbf{\Delta}_t, d_t) := G(\mathbf{\Delta}_t) - d_t \leq 0 \quad \forall t \geq 0 \tag{10}$$

where $G(\mathbf{\Delta}_t)$ is a monotonic loading function which depends on the relative displacement vector $\mathbf{\Delta} = \{\mathbf{\Delta}_1, \mathbf{\Delta}_2, \mathbf{\Delta}_3\}^T$ at time t, and d_t is the damage variable at time t which is used as the threshold function.

The evolution of the damage variable is defined by means of the Kuhn-Tucker constraints which provide the formulation of the loading-unloading–reloading conditions as (Oliver et al. (1990)):

$$\dot{d} \geq 0; \quad F(\boldsymbol{\Delta}_t, d_t) \leq 0; \quad \dot{d} F(\boldsymbol{\Delta}_t, d_t) = 0 \quad \forall t \geq 0 \tag{11}$$

On the other hand, to ensure that the surface of damage activation will grow as much as the internal variable grows, the persistence (or consistency) condition is required. This is:

$$F(\boldsymbol{\Delta}_t, d_t) = 0 \Rightarrow \dot{F}(\boldsymbol{\Delta}_t, d_t) = 0 \quad \forall t \geq 0 \tag{12}$$

Therefore, the damage variable d_t is explicitly defined by:

$$d_t = \max\left\{0, \max_s(G(\boldsymbol{\Delta}_t))\right\} \quad 0 \leq s \leq t \quad \forall t \geq 0 \tag{13}$$

which fully describes the evolution of the internal variable for any loading–unloading–reloading situation. On the other hand, by using the constitutive equation (see Fig. 3) for any mixed-mode ratio β (see Eq. 21), the function $G(\boldsymbol{\Delta}_t)$ is defined as:

$$G(\boldsymbol{\Delta}_t) = \min\left\{\frac{\boldsymbol{\Delta}_t^f(\lambda_t - \boldsymbol{\Delta}_t^o)}{\lambda_t\left(\boldsymbol{\Delta}_t^f - \boldsymbol{\Delta}_t^o\right)}, \, 1\right\} \quad \forall t \geq 0 \tag{14}$$
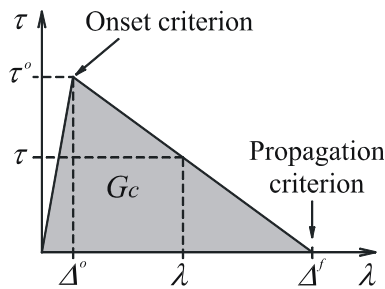

Figure 3: Parameters of the bilinear constitutive equation.

Eq. 14 defines the loading function by means of the bilinear constitutive equation, where $\boldsymbol{\Delta}_t^o$ and $\boldsymbol{\Delta}_t^f$ are the onset and propagation damage parameters at time t, respectively. The values of $\boldsymbol{\Delta}^o$ and $\boldsymbol{\Delta}^f$ are obtained by means of the onset and propagation damage criteria, respectively. These values will be constant unless the mixed-mode ratio changes. The variables used in Eq. 14 are identified in Fig. 3.

2.3 Criterion for damage propagation

The propagation criterion for delamination growth under mixed-mode loading conditions is established in terms of energy release rates and fracture toughnesses. The criterion is based on the work of Benzeggagh and Kenane (1996), and was originally defined for mixed mode I and II:

$$G_c = G_{Ic} + (G_{IIc} - G_{Ic}) \left(\frac{G_{II}}{G_I + G_{II}} \right)^{\eta} \tag{15}$$

where G_{Ic} and G_{IIc} are the fracture toughnesses in mode I and II, respectively; G_I and G_{II} are the energy release rates in mode I and II, respectively. The η parameter is found by least-square fit of experimental data points of fracture toughnesses under different mixed-mode ratios.

The propagation criterion can be rewritten as follows:

$$G_c = G_{Ic} + (G_{shear\_c} - G_{Ic}) B^{\eta} \tag{16}$$

where G_{shear} and G_{shear_c} are the shear energy release rate and the pure mode II fracture toughness, respectively. The expressions of G_{shear} and G_{shear_c} are defined by Eq. 17 and 18, respectively (Camanho et al. (2003)).

$$G_{shear} = G_{II} + G_{III} \tag{17}$$

$$G_{shear\_c} = G_{IIc} (= G_{IIIc}) \tag{18}$$

Eq. 17 is valid whenever the constitutive equations of modes II and III are equal. This hypothesis is very common because the fracture toughness of mode III is difficult to obtain and typically it is considered equal to G_{IIc}.

On the other hand, Eq. 18 ensures that the propagation criterion is consistent for pure mode loading cases II or III. As in the case of Eq. 17, Eq. 18 means that the constitutive equations for mode II and III are equal.

The parameter B is defined as:

$$B = \frac{G_{shear}}{G_I + G_{shear}} \tag{19}$$

The mixed-mode ratio β defined by Turon et al. (2006) is given by:

$$\beta = \frac{\Delta_{shear}}{\langle \Delta_3 \rangle + \Delta_{shear}} \tag{20}$$

However, the definition of β is changed by Eq. 21, which allows the B parameter to be equal to β by developing Eq. 19 and considering the same penalty stiffness for all propagation modes.

$$\beta = \frac{\boldsymbol{\Delta}_{shear}^2}{\langle\boldsymbol{\Delta}_3\rangle^2 + \boldsymbol{\Delta}_{shear}^2} = \frac{\boldsymbol{\Delta}_{shear}^2}{\lambda^2} \tag{21}$$

Finally, the propagation criterion defined in relative displacement terms can be obtained by means of Eq. 16 and by knowing that the crack propagates when the fracture energy release rate is equal to the critical value. In other words, by using Eq. 22 (deduced by means of Eq. 16) and Eq. 23, the propagation criterion yields to Eq. 24.

$$G_c(\beta) = \frac{1}{2}K\boldsymbol{\Delta}_3^o\boldsymbol{\Delta}_3^f + \left(\frac{1}{2}K\boldsymbol{\Delta}_{shear}^o\boldsymbol{\Delta}_{shear}^f - \frac{1}{2}K\boldsymbol{\Delta}_3^o\boldsymbol{\Delta}_3^f\right)\beta^\eta \tag{22}$$

$$G_c(\beta) = \frac{1}{2}K\boldsymbol{\Delta}^o\boldsymbol{\Delta}^f \tag{23}$$

$$\boldsymbol{\Delta}^f = \frac{\boldsymbol{\Delta}_3^o\boldsymbol{\Delta}_3^f + \left(\boldsymbol{\Delta}_{shear}^o\boldsymbol{\Delta}_{shear}^f - \boldsymbol{\Delta}_3^o\boldsymbol{\Delta}_3^f\right)\beta^\eta}{\boldsymbol{\Delta}^o} \tag{24}$$

$\boldsymbol{\Delta}_3^o$ and $\boldsymbol{\Delta}_{shear}^o$ are the relative displacements for damage onset in pure mode I and shear mode respectively, and $\boldsymbol{\Delta}_3^f$ and $\boldsymbol{\Delta}_{shear}^f$ are the relative displacements for damage propagation in pure mode I and shear mode respectively. The parameter $\boldsymbol{\Delta}^o$ is the displacement for damage onset, and it is determined by means of the damage initiation criterion. Normally, the damage propagation criterion is formulated independently of the initiation criterion. However, Eq. 24 shows that both criteria are linked in this model.

2.4 *Criterion for damage onset*

In this model, the criterion for damage onset is assumed the same as the applied criterion for damage propagation. This means that the onset damage criterion is also based on energy terms, which is a different characteristic of the usual cohesive damage formulations where a stress-based criterion is used. The models that account for the interaction of the stress components are usually based on Ye's criterion (1988). However, experimental data of material strengths for the initiation of delamination under mixed-mode loading are not readily available, and consequently, these failure criteria have not been fully validated.

Therefore, by replacing in Eq. 16 only the elastic energy terms of the constitutive equation, Eq. 25 is obtained which is finally equalled to Eq. 26 in order to find the

criterion for damage onset defined in terms of relative displacements (Eq. 27).

$$G_o(\beta) = \frac{1}{2}K(\mathbf{\Delta}_3^o)^2 + \left(\frac{1}{2}K(\mathbf{\Delta}_{shear}^o)^2 - \frac{1}{2}K(\mathbf{\Delta}_3^o)^2\right)\beta^\eta \tag{25}$$

$$\psi(\beta) = \frac{1}{2}K(\mathbf{\Delta}^o)^2 \tag{26}$$

$$\mathbf{\Delta}^o = \left((\mathbf{\Delta}_3^o)^2 + \left((\mathbf{\Delta}_{shear}^o)^2 - (\mathbf{\Delta}_3^o)^2\right)\beta^\eta\right)^{\frac{1}{2}} \tag{27}$$

3 Formulation Adaptations for Non-Zero-Thickness Cohesive Elements

Having formulated a cohesive model for zero-thickness elements, the required modifications to enable also the use of non-zero-thickness elements (i.e. continuum elements) are described in this section.

3.1 Relation between relative displacements and strains

If a continuum element is used, the input data are not the relative displacements, but the strain tensor. Therefore, to model a cohesive continuum model with softening, the relative displacement $\mathbf{\Delta}_i$ and the corresponding strain component ε_{ij} can be related by means of the expression:

$$\mathbf{\Delta}_i = h_e \varepsilon_{ij} n_j (2 - \delta_{3i}) \quad i,j = 1,2,3 \tag{28}$$

where h_e is the element thickness, and n_j is the corresponding component of the unitary normal vector to the crack plane, $\mathbf{n} = \{0,0,1\}^T$ (see Fig. 2).

As explained in the model formulation, the area under the constitutive equation g_e defined by stresses and relative displacements is directly the fracture toughness of the material G_c. However, if the constitutive model is defined in terms of stresses and strains, the law has to be adjusted in function of the element thickness h_e. Then, the resultant area g_e is the dissipated energy by unit of volume at the corresponding integration point of the finite element. This energy is equal to the fracture toughness of the material divided by the finite element thickness (see Eq. 29). This approach follows the called Crack Band Model suggested by Bažant and Oh (1983), which is the procedure normally used to ensure the correct energy dissipation and mesh independency in continuum damage models.

$$E = G_c A_{crack} = g_e(A_{crack}h_e) \quad \Rightarrow \quad g_e = \frac{G_c}{h_e} \tag{29}$$

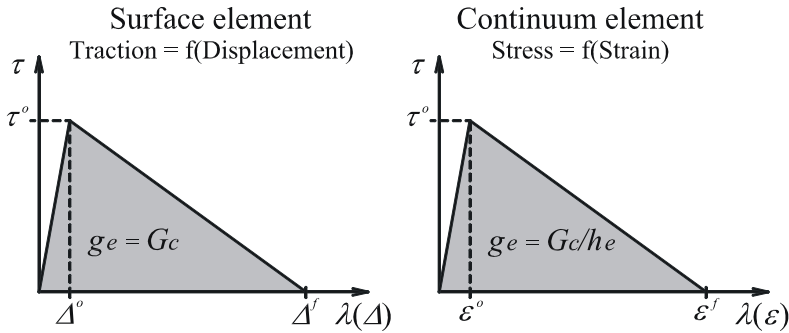The dissipated energies for each case are illustrated in Fig. 4.

Figure 4: Constitutive charts defined by stresses and relative displacements (left), or by stresses and strains (right).

3.2   Penalty stiffness

If cohesive volumetric elements are used, the penalty stiffness is here varied in function of the mixed-mode ratio. Its definition can be done in function of the element thickness and the elastic properties of the modelled interface material (Allix et al. (1995)). In particular, Eq. 30 defines the penalty stiffness for pure mode I, and Eq. 31 defines the penalty stiffness for pure modes II or III (shear):

$$K_1 = \frac{E_m}{h_e} \tag{30}$$

$$K_2 = \frac{G_m}{h_e} \tag{31}$$

where E_m is the Young's modulus and G_m is the shear elastic modulus of the interface material. Normally, the elastic properties of the interface material are considered as the neat material, although it is generally not true (Corigliano and Allix (2000)).

For surface cohesive elements, the penalty stiffness is selected with a fixed value for all mixed-mode ratios. Ideally, the value of the penalty stiffness is infinite because these elements do not have thickness, and then they do not affect the compliance of the whole structure (Remmers et al. (2003)). However, too high value of the interface stiffness can generate numerical problems such as the generation of spurious oscillations in the tractions of the element (Schellekens and De Borst (1993)). Therefore, a suitable value of the penalty stiffness should be selected in order to provide a reasonable stiffness without generating numerical problems. Based in mechanical considerations, Turon et al. (2007) proposed Eq. 32 in order to esti-

mate the interface stiffness K for mode I crack propagation.

$$K = \frac{\alpha E_{33}}{t} \tag{32}$$

E_{33} is the elastic modulus through-the-thickness of the composite material, α is an increasing parameter (normally it is taken about $\alpha \approx 50$), and t is the laminate thickness adjoining to the cohesive element. Eq. 32 also can be developed for shear modes, by replacing E_{33} by the shear elastic modulus. However, since the model formulation for surface elements assumes the same penalty stiffness for each mixed-mode ratio, Eq. 32 is used for all cases because it gives the biggest value.

3.3 Redefined onset and propagation damage criteria

Since the penalty stiffness for the volumetric elements is a function of the mixed-mode ratio, the onset and propagation damage criteria written in terms of relative displacements must be redefined. However, the procedure used in sections 2.3 and 2.4 to find these expressions can not be exactly applied here because the function which describes the variation of the penalty stiffness under a determined mixed-mode ratio is unknown.

In order to find the onset criterion, Eq. 33 is used. This equation is the damage criterion with the corresponding elastic energy terms replaced (i.e. Eq. 25 with different penalty stiffness for pure mode I and pure shear mode). On the other hand, Eq. 34 represents the elastic energy of the constitutive equation defined in terms of relative displacements of pure mode I, $\boldsymbol{\Delta}_3^o(\beta)$, and pure shear mode, $\boldsymbol{\Delta}_{shear}^o(\beta)$, for damage onset in a determined mixed-mode ratio.

$$G_o(\beta) = \frac{1}{2} K_1 \left(\boldsymbol{\Delta}_3^o\right)^2 + \left(\frac{1}{2} K_2 \left(\boldsymbol{\Delta}_{shear}^o\right)^2 - \frac{1}{2} K_1 \left(\boldsymbol{\Delta}_3^o\right)^2\right) B^\eta \tag{33}$$

$$\psi(\beta) = \frac{1}{2} K_1 \langle \boldsymbol{\Delta}_3^o(\beta)\rangle^2 + \frac{1}{2} K_2 \left(\boldsymbol{\Delta}_{shear}^o(\beta)\right)^2 \tag{34}$$

Using Eq. 33 and 34, and the selected definition of the mixed-mode ratio (Eq. 21), the terms $\boldsymbol{\Delta}_3^o(\beta)$ and $\boldsymbol{\Delta}_{shear}^o(\beta)$ can be found:

$$\langle \boldsymbol{\Delta}_3^o(\beta)\rangle = \left(\frac{2 G_o(\beta)}{K_1 + \left(\frac{\beta}{1-\beta}\right) K_2}\right)^{\frac{1}{2}} \tag{35}$$

$$\boldsymbol{\Delta}_{shear}^o(\beta) = \left(\frac{\beta}{1-\beta}\right)^{\frac{1}{2}} \langle \boldsymbol{\Delta}_3^o(\beta)\rangle \tag{36}$$

Finally, the onset damage criterion is obtained by taking the Euclidian norm of the relative displacements described by Eq. 35 and 36 (see section 2.1):

$$\Delta^o = \left(\langle \Delta_3^o (\beta) \rangle^2 + (\Delta_{shear}^o (\beta))^2 \right)^{\frac{1}{2}} \tag{37}$$

In the same sense, the propagation damage criterion can be deduced. In this case, Eq. 38 represents the damage criterion with the corresponding pure fracture toughness terms replaced (i.e. Eq. 22 with different penalty stiffness for pure mode I and pure shear mode). On the other hand, Eq. 39 is the fracture toughness for a given mixed-mode ratio defined in terms of relative displacements for damage onset in pure modes I and shear, $\Delta_3^o (\beta)$ and $\Delta_{shear}^o (\beta)$, and for damage propagation, $\Delta_3^f (\beta)$ and $\Delta_{shear}^f (\beta)$.

$$G_c (\beta) = \frac{1}{2} K_1 \Delta_3^o \Delta_3^f + \left(\frac{1}{2} K_2 \Delta_{shear}^o \Delta_{shear}^f - \frac{1}{2} K_1 \Delta_3^o \Delta_3^f \right) B^\eta \tag{38}$$

$$G_c (\beta) = \frac{1}{2} K_1 \langle \Delta_3^o (\beta) \rangle \left\langle \Delta_3^f (\beta) \right\rangle + \frac{1}{2} K_2 (\Delta_{shear}^o (\beta)) \left(\Delta_{shear}^f (\beta) \right) \tag{39}$$

where $\Delta_3^o (\beta)$ and $\Delta_{shear}^o (\beta)$ are previously found by means of Eq. 35 and 36.

By equalling Eq. 38 and 39, and by using again the definition of the mixed-mode ratio (Eq. 21), the terms $\Delta_3^f (\beta)$ and $\Delta_{shear}^f (\beta)$ can be found:

$$\left\langle \Delta_3^f (\beta) \right\rangle = \frac{K_1 (1 - B^\eta) \Delta_3^o \Delta_3^f + K_2 B^\eta \Delta_{shear}^o \Delta_{shear}^f}{\langle \Delta_3^o (\beta) \rangle \left(K_1 + \left(\frac{\beta}{1-\beta} \right) K_2 \right)} \tag{40}$$

$$\Delta_{shear}^f (\beta) = \left(\frac{\beta}{1-\beta} \right)^{\frac{1}{2}} \left\langle \Delta_3^f (\beta) \right\rangle \tag{41}$$

Finally, the propagation damage criterion is obtained by making the Euclidian norm of the relative displacements described by Eq. 40 and 41 (see section 2.1):

$$\Delta^f = \left(\left\langle \Delta_3^f (\beta) \right\rangle^2 + \left(\Delta_{shear}^f (\beta) \right)^2 \right)^{\frac{1}{2}} \tag{42}$$

It should be noted that the B parameter must be redefined by Eq. 43, since the penalty stiffnesses in pure mode I and shear modes are different and then they can not be simplified.

$$B = \frac{K_2 \beta}{K_2 \beta + K_1 (1-\beta)} \tag{43}$$

If Eq. 30 and 31 are replaced in Eq. 43, the *B* parameter can be also defined in function of the elastic properties considered for the interface material. That is:

$$B = \frac{G_m \beta}{G_m \beta + E_m (1 - \beta)} \tag{44}$$

4   Model Implementation

4.1   Strategy of implementation

The delamination model presented by Turon et al. (2006) was implemented in a user-written element subroutine called UEL (Abaqus 6.8 (2008)). This implementation was used to simulate problems in an implicit finite element code. However, the model formulated in sections 2 and 3 is here implemented in a user-written material subroutine, called VUMAT, assigned for explicit finite element analysis.

The user material implemented has to be defined on sets of elements which represent the delamination layers. These elements can be zero-thickness (i.e. surface elements) or non-zero-thickness (i.e. continuum elements) types. In particular, when a zero-thickness interface is used, in-plane cohesive elements with four integration points of the Abaqus element library must be used (Aymerich et al. (2008)). This element is called COH3D8. However, when non-zero-thickness interface is desired, any tri-dimensional solid element can be applied.

When surface elements are used, the input data given by the finite element software to the user material subroutine is directly the increment of the relative displacement vector, whereas the input data for continuum elements is the increment of the strain tensor. In order to use the same subroutine for both element types, Eq. 28 is applied to transform easily the corresponding strain tensor components to relative displacements (see Fig. 5). On the other hand, if surface elements are used, a constitutive thickness equal to the unity has to be introduced in the user material subroutine which ensures that the strains are equal to the relative displacements.

4.2   Input variables to define the model in a user material subroutine

The parameters required to define completely the model in a user material subroutine are described below:

- Elastic properties and density of the interface material (isotropic): E_m, ν_m and ρ_m.

  By means of E_m and ν_m the value of G_m can by calculated by using Eq. 45. If surface elements are used, normally the value of E_m is taken between 10^5 and 5e6 N/mm³ for a sub-laminate thickness between 0.125 mm and 5 mm
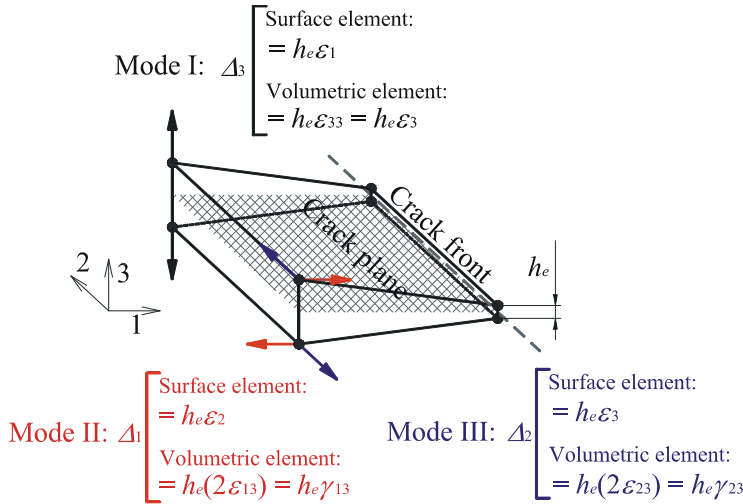
Figure 5: Transformations from strains to relative displacements for each propagation mode.

(Turon et al. (2007)), and the Poisson coefficient v_m must be equal to -0.5 in order to obtain the same penalty stiffness for all mixed-mode ratios.

$$G_m = \frac{E_m}{2(1+v_m)} \tag{45}$$

- Thickness of the interface cohesive element: h_e.

  If surface elements are used, the value of the constitutive thickness introduced in the subroutine must be equal to the unity (although the geometrical thickness defined in the model is equal to zero).

- Interface strengths for pure mode I and shear modes (II and III): τ_3^o and τ_1^o.

  The relative displacements which give the damage onset for pure mode loading cases are obtained by means of the interface strengths. The corresponding equations are:

$$\Delta_3^o = \frac{\tau_3^o}{K_1} \tag{46}$$

$$\Delta_{shear}^o = \frac{\tau_1^o}{K_2} \tag{47}$$

- Interface fracture toughness for pure mode I and shear modes (II and III): G_{Ic} and G_{IIc}.

  The relative displacements which give the damage propagation for pure mode loading cases are obtained by means of pure mode fracture toughnesses. The corresponding equations are:

$$\Delta_3^f = \frac{2G_{Ic}}{K_1 \Delta_3^o} = \frac{2G_{Ic}}{\tau_3^o} \tag{48}$$

$$\Delta_{shear}^f = \frac{2G_{IIc}}{K_2 \Delta_{shear}^o} = \frac{2G_{IIc}}{\tau_1^o} \tag{49}$$

- Parameter of the least-square fit: η.

  The experimental data used to calculate η is obtained from MMB tests (Mixed-Mode Bending) at different mode ratios.

4.3 Algorithm

The steps of the algorithm implemented in the user material subroutine repeated for each stable time increment Δt are numbered below:

0. Read the properties defined and calculate the model parameters (see previous sections 3.2 and 4.2).

1. Calculate the strain components at time $t + \Delta t$.

$$\varepsilon_{i_{t+\Delta t}} = \varepsilon_{i_t} + \Delta \varepsilon_{i_{t+\Delta t}} \begin{cases} i = 1, ..., 3 & (surface\,element) \\ i = 1, ..., 6 & (volumetric\,element) \end{cases} \tag{50}$$

2. Calculate the relative displacements at time $t + \Delta t$ for each propagation mode.

$$
\begin{aligned}
Mode\,I: \quad & \Delta_{3t+\Delta t} = \begin{cases} h_e \varepsilon_{1t+\Delta t} & (surface\,element) \\ h_e \varepsilon_{3t+\Delta t} & (volumetric\,element) \end{cases} \\[6pt]
Mode\,II: \quad & \Delta_{1t+\Delta t} = \begin{cases} h_e \varepsilon_{2t+\Delta t} & (surface\,element) \\ h_e \gamma_{13t+\Delta t} & (volumetric\,element) \end{cases} \\[6pt]
Mode\,III: \quad & \Delta_{2t+\Delta t} = \begin{cases} h_e \varepsilon_{3t+\Delta t} & (surface\,element) \\ h_e \gamma_{23t+\Delta t} & (volumetric\,element) \end{cases}
\end{aligned} \tag{51}
$$

3. Application of the damage model, where the following terms are calculated:

$$\mathbf{\Delta}_{shear_{t+\Delta t}} = \sqrt{\left(\mathbf{\Delta}_{1t+\Delta t}\right)^2 + \left(\mathbf{\Delta}_{2t+\Delta t}\right)^2} \tag{52}$$

$$\lambda_{t+\Delta t} = \sqrt{\left\langle \mathbf{\Delta}_{3t+\Delta t}\right\rangle^2 + \left(\mathbf{\Delta}_{shear_{t+\Delta t}}\right)^2} \tag{53}$$

$$\beta_{t+\Delta t} = \frac{\mathbf{\Delta}^2_{shear_{t+\Delta t}}}{\left\langle \mathbf{\Delta}_{3t+\Delta t}\right\rangle^2 + \mathbf{\Delta}^2_{shear_{t+\Delta t}}} \tag{54}$$

$$B_{t+\Delta t} = \frac{K_2 \beta_{t+\Delta t}}{K_2 \beta_{t+\Delta t} + K_1 \left(1 - \beta_{t+\Delta t}\right)} \tag{55}$$

$$\left\langle \mathbf{\Delta}_3^o(\beta)\right\rangle_{t+\Delta t} = \left(\frac{K_1 \left(1 - B_{t+\Delta t}^{\eta}\right)\left(\mathbf{\Delta}_3^o\right)^2 + K_2 B_{t+\Delta t}^{\eta}\left(\mathbf{\Delta}_{shear}^o\right)^2}{K_1 + \left(\frac{\beta_{t+\Delta t}}{1-\beta_{t+\Delta t}}\right)K_2}\right)^{\frac{1}{2}} \tag{56}$$

$$\left\langle \mathbf{\Delta}_3^f(\beta)\right\rangle_{t+\Delta t} = \frac{K_1 \left(1 - B_{t+\Delta t}^{\eta}\right)\mathbf{\Delta}_3^o \mathbf{\Delta}_3^f + K_2 B_{t+\Delta t}^{\eta}\mathbf{\Delta}_{shear}^o \mathbf{\Delta}_{shear}^f}{\left\langle \mathbf{\Delta}_3^o(\beta)\right\rangle_{t+\Delta t}\left(K_1 + \left(\frac{\beta_{t+\Delta t}}{1-\beta_{t+\Delta t}}\right)K_2\right)} \tag{57}$$

$$\left(\mathbf{\Delta}_{shear}^f(\beta)\right)_{t+\Delta t} = \left(\frac{\beta_{t+\Delta t}}{1 - \beta_{t+\Delta t}}\right)^{\frac{1}{2}} \left\langle \mathbf{\Delta}_3^f(\beta)\right\rangle_{t+\Delta t} \tag{58}$$

$$\mathbf{\Delta}^o_{t+\Delta t} = \left(\left\langle \mathbf{\Delta}_3^o(\beta)\right\rangle_{t+\Delta t}^2 + \left(\mathbf{\Delta}_{shear}^o(\beta)\right)_{t+\Delta t}^2\right)^{\frac{1}{2}} \tag{59}$$

$$\mathbf{\Delta}^f_{t+\Delta t} = \left(\left\langle \mathbf{\Delta}_3^f(\beta)\right\rangle_{t+\Delta t}^2 + \left(\mathbf{\Delta}_{shear}^f(\beta)\right)_{t+\Delta t}^2\right)^{\frac{1}{2}} \tag{60}$$

$$G(\mathbf{\Delta}_{t+\Delta t}) = \min\left\{\frac{\mathbf{\Delta}^f_{t+\Delta t}\left(\lambda_{t+\Delta t} - \mathbf{\Delta}^o_{t+\Delta t}\right)}{\lambda_{t+\Delta t}\left(\mathbf{\Delta}^f_{t+\Delta t} - \mathbf{\Delta}^o_{t+\Delta t}\right)}, 1\right\} \tag{61}$$

- If $G(\mathbf{\Delta}_{t+\Delta t}) \leq d_t \quad \Rightarrow \quad d_{t+\Delta t} = d_t$
  $\rightarrow$ Elastic reloading, unloading or neutral loading.
- If $G(\mathbf{\Delta}_{t+\Delta t}) > d_t \quad \Rightarrow \quad d_{t+\Delta t} = G(\mathbf{\Delta}_{t+\Delta t})$
  $\rightarrow$ Loading.

4. Calculate the stress vector at time $t + \Delta t$:

$$\tau_{t+\Delta t} = C_{t+\Delta t}\varepsilon_{t+\Delta t} \tag{62}$$

where:

- For surface elements:

$$C_{t+\Delta t} = \begin{bmatrix} \left(1-d^*_{t+\Delta t}\right)E_m & 0 & 0 \\ 0 & \left(1-d_{t+\Delta t}\right)G_m & 0 \\ 0 & 0 & \left(1-d_{t+\Delta t}\right)G_m \end{bmatrix} \tag{63}$$

where:

$$d^*_{t+\Delta t} = d_{t+\Delta t}\frac{\left\langle \varepsilon_{1_{t+\Delta t}}\right\rangle}{\left|\varepsilon_{1_{t+\Delta t}}\right|} \tag{64}$$

- For volumetric elements:

$$C_{t+\Delta t} = \left[\begin{array}{cc} \dfrac{E_m\left(1-\left(1-d^*_{t+\Delta t}\right)v_m^2\right)}{\Upsilon} & -\dfrac{v_m E_m\left(-1-\left(1-d^*_{t+\Delta t}\right)v_m\right)}{\Upsilon} \\ -\dfrac{v_m E_m\left(-1-\left(1-d^*_{t+\Delta t}\right)v_m\right)}{\Upsilon} & \dfrac{E_m\left(1-\left(1-d^*_{t+\Delta t}\right)v_m^2\right)}{\Upsilon} \\ \dfrac{v_m E_m\left(1-d^*_{t+\Delta t}\right)}{\Phi} & \dfrac{v_m E_m\left(1-d^*_{t+\Delta t}\right)}{\Phi} \\ 0 & 0 \\ 0 & 0 \\ 0 & 0 \end{array} \right.$$

$$\left. \begin{array}{cccc} \dfrac{v_m E_m\left(1-d^*_{t+\Delta t}\right)}{\Phi} & 0 & 0 & 0 \\ \dfrac{v_m E_m\left(1-d^*_{t+\Delta t}\right)}{\Phi} & 0 & 0 & 0 \\ -\dfrac{E_m\left(1-d^*_{t+\Delta t}\right)(1-v_m)}{\Phi} & 0 & 0 & 0 \\ 0 & G_m & 0 & 0 \\ 0 & 0 & \left(1-d_{t+\Delta t}\right)G_m & 0 \\ 0 & 0 & 0 & \left(1-d_{t+\Delta t}\right)G_m \end{array} \right] \tag{65}$$

where:

$$\Phi = 1 - 2v_m^2\left(1-d^*_{t+\Delta t}\right) - v_m \tag{66}$$

$$\Upsilon = 1 - 2v_m^3\left(1-d^*_{t+\Delta t}\right) - v_m^2\left(3-2d^*_{t+\Delta t}\right) \tag{67}$$

$$d^*_{t+\Delta t} = d_{t+\Delta t}\frac{\left\langle \varepsilon_{3_{t+\Delta t}}\right\rangle}{\left|\varepsilon_{3_{t+\Delta t}}\right|} \tag{68}$$

5. Calculate the energy dissipated at time $t+\Delta t$:

$$D_{t+\Delta t} = D_t + D_{\Delta t} \tag{69}$$

where D_t and $D_{\Delta t}$ are the accumulated and the increment of the dissipated energy, respectively. The determination of $D_{\Delta t}$ is given by Eq. 70:

$$D_{\Delta t} = \frac{1}{2}\left(\frac{d_{t+\Delta t}-d_t}{\Delta t}\right)\left(K_1\left(\Delta^2_{3_{t+\Delta t}}+\Delta_{3_{t+\Delta t}}\left\langle -\Delta_{3_{t+\Delta t}}\right\rangle\right) + K_2\left(\Delta^2_{1_{t+\Delta t}}+\Delta^2_{2_{t+\Delta t}}\right)\right) \tag{70}$$

6. Calculate the free energy at time $t + \Delta t$.

$$\psi_{t+\Delta t} = \frac{1}{2}\left((1 - d_{t+\Delta t})\left(K_2\left(\Delta^2_{1_{t+\Delta t}} + \Delta^2_{2_{t+\Delta t}}\right) + K_1\left(\Delta^2_{3_{t+\Delta t}}\right)\right)\right.$$
$$\left. - d_{t+\Delta t}K_1\left(\Delta_{3_{t+\Delta t}}\left\langle -\Delta_{3_{t+\Delta t}}\right\rangle\right)\right) \quad (71)$$

7. Calculate the internal energy at time $t + \Delta t$.

$$U_{t+\Delta t} = \psi_{t+\Delta t} + D_{t+\Delta t} \quad (72)$$

5   Dimensions of Cohesive Elements

5.1   *Maximum thickness of volumetric cohesive elements*

For each mixed-mode ratio there is a maximum thickness of the cohesive elements in the direction perpendicular to the crack propagation plane. This is due to the fact that the propagation criterion defined in terms of relative displacements remains constant and the onset criterion changes whether the element thickness changes. The reason of the onset criterion changes is due to the introduction of penalty stiffness dependency with element thickness (see Eq. 30 and 31). Since the onset criterion should be reached before the propagation criterion, equalizing both criteria the maximum cohesive thickness $h_{e,max}$ is obtained for a given mixed-mode ratio β. The resulting equation which defines the maximum thickness of the cohesive element, $h_{e,\max}$, is:

$$h_{e,\,\max} = \frac{2\left(G_{Ic} + (G_{IIc} - G_{Ic})B^{\eta}\right)}{\frac{(\tau_3^o)^2}{E_m} + \left(\frac{(\tau_1^o)^2}{G_m} - \frac{(\tau_3^o)^2}{E_m}\right)B^{\eta}} \quad (73)$$

By means of Eq. 73 it is possible to plot the variation of the maximum cohesive element thickness as a function of the mixed-mode ratio, which is included in parameter B by Eq. 43. Taken into account the material properties shown in Tab. 2 and 3, the evolution of the maximum thickness is plotted in Fig. 6.

Eq. 73 can also be obtained by using the onset and propagation criteria defined in terms of strains. In this case, the onset criterion remains constant versus the variations of the thickness, whereas the propagation criterion changes in order to assess the correct energy dissipation independently of the mesh size.

Normally, the cohesive element thickness is defined with a small value (e.g. between 0.001 and 0.1 mm) and certainly the value used will be smaller than the maximum value given by Eq. 73.
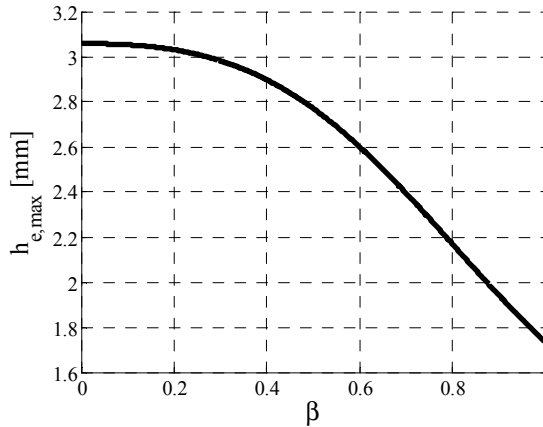
Figure 6: Evolution of the maximum element thickness in function of the mixed-mode ratio.

Using again the material properties shown in Tab. 2 and 3, the variation of the onset criterion of the constitutive equation defined in terms of relative displacements and the variation of the propagation criterion of the constitutive equation chart defined in terms of strains are shown in Fig. 7. These charts correspond to the simulations in one element with constant in-plane dimensions under pure mode I loading.
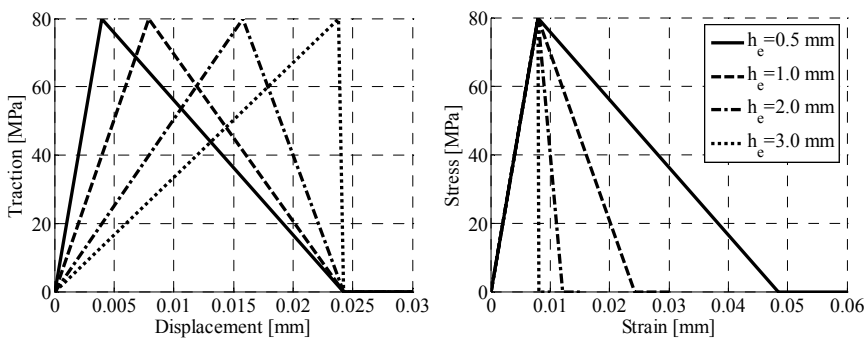

Figure 7: Constitutive equation charts defined by relative displacements and strains in function of the element thickness.

5.2   In-plane dimensions of the cohesive elements

The in-plane dimensions of the cohesive elements are selected following the considerations and equations proposed by Turon et al. (2007). In particular, the in-plane dimensions are defined by means of the cohesive zone length l_{cz}, which is a material and structural property (Yang and Cox (2005)). It is defined as the distance from the crack front until the point with the maximum interface strength τ^o. To obtain suitable results by using cohesive zone models, the tractions in the cohesive zone have to be represented correctly by a proper number of elements.

The model that will be used in this paper in order to predict the length of the cohesive zone was proposed by Rice (1980), and reads:

$$l_{cz} = \frac{9\pi}{32} E_m \frac{G_c(\beta)}{(\tau^o(\beta))^2} \tag{74}$$

where E_m is the Young's modulus, and $G_c(\beta)$ and $\tau^o(\beta)$ are the fracture toughness and the maximum strength of the interface for a given mixed-mode ratio, respectively.

The length of the cohesive elements l_e is easily calculated by means of:

$$l_e = \frac{l_{cz}}{N_e} \tag{75}$$

where N_e is the number of elements in the cohesive zone. Normally, the smallest value of the cohesive zone length resulted from the different values of mixed-mode ratio is used, and it is recommended to apply at least three or four elements in order to describe the cohesive zone accurately.

6   Simulations

This section presents the application of cohesive elements in the simulation of interlaminar fracture tests of composite specimens under quasi-static loading conditions. These tests allow the validation of the damage model presented without consider the interaction with other damage mechanisms which can appear inside the layers, because the damage is normally concentrated in interfaces where only delamination occurs.

First, Mixed-Mode Bending (MMB) and End-Notched Flexure (ENF) tests of unidirectional zero degree layup specimens with an initial pre-crack are considered (see section 6.2). The MMB allows to test any mixed-mode case except pure mode II, which is obtained by the ENF test. The cases simulated are $B =0.0$ (pure mode I), $B =0.2$, $B =0.5$, $B =0.8$ and $B =1.0$ (pure mode II). It should be noted that

only non-zero-thickness elements have been used in all the simulations considered, which represent a resin-rich interface layer.

Different mixed-mode analyses at one finite element were simulated previously in order to check that the predicted dissipated energy at each integration point is equal to the corresponding fracture toughness adjusted by the least square fit of experimental data points of the selected material (see Tab. 3).

Simulations of quasi-static Transverse Crack Tension tests (TCT) of unidirectional zero degree layup specimens are also shown (see section 6.3). The TCT test is an alternative to the ENF test, which determines pure mode II interlaminar fracture toughness (Prinz and Cao (1989)).

Finally, the numerical considerations in order to carry out quasi-static simulations by using an explicit finite element code are explained in detail.

6.1 Model considerations for quasi-static explicit simulations

The proposed simulations are solved by means of an explicit finite element code. As it has been explained in the introduction, the explicit integration schemes determine a solution to the dynamic equilibrium of the global set equations by explicitly advancing the kinematic state from the previous time increment, without solving simultaneously equations and without iterating for each time increment. For this reason, the formulation of the tangent stiffness tensor is not derived since no iterations are carried out. Therefore, the accelerations, velocities and displacements are calculated explicitly at each node recurring to a simple central differences rule applied over a time increment.

For linear and nonlinear problems alike, explicit methods require a small time increment size which is independent of the type and duration of loading, and depends solely on the highest natural frequency $\omega_{\max}$ and on the critical damping ξ in the mode with the highest frequency. That is:

$$\Delta t_{stable} \leq \frac{2}{\omega_{\max}} \left(\xi \sqrt{1 + \xi^2} \right) \tag{76}$$

Alternately, instead of looking at the global model, a simple estimate which is efficient and conservative can be used. It is based on the highest frequency of each individual finite element of the model, which is always associated with the dilatational mode. It can be shown that the highest element frequency determined is always higher than the highest frequency in the assembled finite element model. Then, this method is more conservative, because it will give a smaller stable time increment than the true stability limit that is based on the maximum frequency of the entire model. Based on these observations, the stability limit can be approached

by means of the called Courant condition which considers the minimum dimension of the element L_e and the wave speed of the material c_m:

$$\Delta t_{stable} \leq \frac{L_e}{c_m} \tag{77}$$

where the wave speed is a material property:

$$c_m = \sqrt{\frac{E_m}{\rho_m}} \tag{78}$$

where E_m and ρ_m represent the bulk stiffness and the density, respectively, of the interface material (Bergan and Mollestad (1985); Abaqus 6.8 (2008)).

Eq. 77 shows that the stable time increment is roughly proportional to the shortest element dimension, and then it is advantageous to keep the element size as large as possible. However, the use of cohesive elements reduces the time increment due to their small thickness. There are some actions to alter one or more of the factors influencing the time increment. The action here considered for increasing the efficiency of the proposed simulations is to scale the mass density of these critical elements (i.e. mass scaling).

Static problems have a large time solution, which often it is unworkable to analyze the simulation in its real scale of time using an explicit code because requires an excessive number of stable small increments of time. To obtain a faster solution, the event should be accelerated in some way, but ensuring that the inertial forces remain insignificant. With the use of Rayleigh damping and a modification to the density, a solution to a non-linear static problem can be obtained in a realistic time (Iannucci (2006)). In order to control the proposed simulations, the kinetic energy and the internal energy are monitored in order to keep the kinetic energy less than 5% of the internal energy of the system. This is sometimes referenced to as dynamic relaxation (Papadrakakis (1981); Sauvé and Metzger (1995)).

On the other hand, the loading velocity should be such that the solution obtained is close to the real static solution and the dynamic effects remain insignificant. In an approximate way, the maximum loading velocity could be estimated by means of:

$$v_L < 0.01 \sqrt{\frac{E_m}{\rho_m}} \tag{79}$$

The loading velocity defined in all the simulations is 0.5 mm/s, which is much lower than the maximum value given by Eq. 79 (see interface properties in Tab. 2 and 7).

Quasi-static analyses in explicit algorithms require the application of loading as smooth as possible. Sudden movements cause stress waves, which can introduce noisy or inaccurate results. Applying the load in the smoothest possible manner requires that the acceleration changes only a small amount from one time increment to the next. Then, if the acceleration is smooth, it follows that the changes in velocity and displacement are also smooth. This option can be defined easily in Abaqus software by selecting a smooth amplitude table of loading in all the proposed simulations. By defining it, Abaqus software connects automatically each of the user data pairs of loading with curves, whose first and second derivatives are smooth, and whose values are zero at each of user loading data points (Abaqus 6.8 (2008)).

It has to be noted that the selected mass scaling factor for critical elements is considerably high ($\approx 1.0e3$). However, since the boundary displacements are applied in a smooth manner and in a large time scale, the kinetic energy and the inertial forces of the model remain small.

In all simulations proposed, Rayleigh Damping is applied, which damps lower (i.e. mass-dependent) and higher (i.e. stiffness-dependent) frequency range behaviours. Rayleigh Damping is defined by means of two damping factors: the mass proportional damping α_R which damps the lower frequencies, and the stiffness proportional damping β_R which damps the higher frequencies. The mass proportional damping factor introduces damping forces caused by the absolute velocities of the model and so simulates the model moving through a viscous media. A mass proportional damping factor is adopted in order to improve the dynamic simulation to a quasi-static solution. In all the simulations, the value defined is set to critically damp the lowest frequency of the model (Abaqus 6.8 (2008)). On the other hand, the stiffness proportional damping factor adds damping stress to the stress caused by the constitutive response at the integration point. However, in all simulations the high frequency noise expected is not observed probably due to the viscosity coefficients used to control the unrealistic hourglass modes generated from single integration elements and also by the default introduction of a small amount of numerical damping in the form of bulk viscosity to control high frequency oscillations (Iannucci (2006)). Therefore, no stiffness proportional Rayleigh damping is defined which it is favourable consideration since this factor often implies a dramatic drop in the stable time increment.

Finally, the cohesive elements which reach the maximum damage value at their integration points are deleted from the mesh. These deleted elements have no ability to carry stresses and, therefore, have no contribution to the stiffness of the model. This action avoids large deformations of the damaged elements, and possible spurious stress transfer to the bodies around them. However, if damaged elements are

deleted, penetration between the joined laminates can occur, mainly in tests with high percentage of mode II. To avoid it, a contact pair surfaces without friction have been defined between the two laminate surfaces that were initially linked by the cohesive elements.

6.2 MMB and ENF fracture toughness tests

The simulations of quasi-static MMB and ENF tests of unidirectional zero degree layup specimens are analysed in this section.

6.2.1 Configuration of the tests

The loading conditions in the MMB simulations are defined by means of the linear Eq. 80 which relates the displacements in three different points of the specimen (Camanho et al. (2003)):

$$\Lambda_{LP} = \left(\frac{c}{L}\right)\Lambda_I + \left(\frac{c+L}{L}\right)\Lambda_M \tag{80}$$

where L is the half specimen length and c is the length from the loading point (LP) to the middle point (M) of the specimen. The different mixed-mode cases are generated by modifying the length c, which reads:

$$c = \frac{L\left(\frac{1}{2}\sqrt{3\left(\frac{1-B}{B}\right)}+1\right)}{3-\frac{1}{2}\sqrt{3\left(\frac{1-B}{B}\right)}} \tag{81}$$

In Fig. 8 are marked the points LP, M, and I where the displacements are pre-scribed.
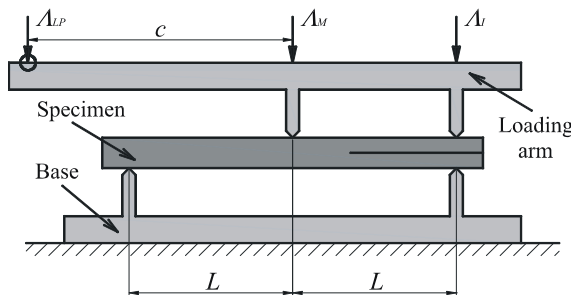
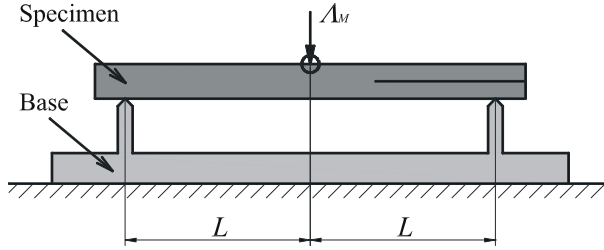

Figure 8: MMB test configuration.

Figure 9: ENF test configuration.

The loading conditions of the ENF test are also defined by displacements. Just as indicates Fig. 9, it is applied a displacement in the middle point M of the specimen.

The numerical results are compared with experimental data performed by Reeder and Crews (1990, 1991 and 1998) to validate the model. These results are presented in a force-displacement chart. For the MMB test, the results are read at point LP (Fig. 8), and in point M for the ENF test (Fig. 9).

6.2.2 Sizes and types of the elements

An 8-node solid element with reduced integration (one integration point) is used to model the laminates and volumetric cohesive elements. This element is called C3D8R (Abaqus 6.8 (2008)). For all simulations, each laminate thickness is modelled by four elements, which is enough to capture accurately the laminate rotations during the simulations. The thickness defined for the interface elements is 0.01 mm, which is much smaller than the value obtained by means of Eq. 73 (see Fig. 6).

On the other hand, the in-plane length of the cohesive element is determined by Eq. 74 and 75. If three elements are desired to be along the cohesive length, the maximum in-plane length at the crack propagation direction is of 0.45 mm. The length finally used is 0.3 mm for all the simulations. It is not necessary to define a small length element at width specimen direction because the crack propagates on the opposite direction. Therefore, the specimen width is modelled by using only two elements.

6.2.3 Materials and specimen dimensions

The material used is a thermoplastic matrix-based reinforced by unidirectional carbon fibres (AS4/PEEK). The properties are set in Tab. 1.

The material properties defined to the interface elements are defined in Tab. 2, and are selected by considering that these elements represent a resin-rich layer. The

Table 1: AS4/PEEK properties.

E_{11} (MPa)	$E_{22} = E_{33}$ (MPa)	$G_{12} = G_{13}$ (MPa)	G_{23} (MPa)	$v_{12} = v_{13}$	v_{23}	ρ (t/mm^3)
122700	10100	5500	3700	0.25	0.45	1600e-12

pure mode fracture toughnesses (see section 4.2) of the interface are written in Tab. 3.

Table 2: Interface properties.

E_m (MPa)	v_m	ρ_m (t/mm^3)	τ_3^o (MPa)	$\tau_1^o = \tau_2^o$ (MPa)
10100	0.3	1600e-12	80	100

Table 3: Fracture toughnesses of the interface for different mixed-mode ratios (Reeder and Crews (1991 and 1998)).

G_{II}/G_T	0% (*MMB*)	20% (*MMB*)	50% (*MMB*)	80% (*MMB*)	100% (*MMB*)
G_c (N/mm)	0.969	1.103	1.131	1.376	1.719
Initial crack length: a_0(mm)	32.9	33.7	34.1	31.4	39.2

The parameter η is taken 2.284, which is obtained by means of a least-square fit of the experimental data exposed in Tab. 3.

The specimen dimensions are: 102 mm long, 25.4 mm wide, and each laminate arm is 1.56 mm thick.

6.2.4 Results

The force-displacement relations obtained in the experiments and in the finite element simulations of the MMB test for each proposed mixed-mode case: $B = 0.0$ (pure mode I), $B = 0.2$, $B = 0.5$, and $B = 0.8$ are respectively shown in Fig. 10, 11, 12, 13. The results of the ENF test ($B = 1.0$, pure mode II) are shown in Fig. 14.

The corresponding analytical expressions for MMB test with $B = 0.0$ (pure mode I) and ENF test which give the relationship of the critical load and the displacement during propagation are also plotted in the corresponding figures. These equations

are set in Tab. 4 and 5, and are deduced by using Linear Elastic Fracture Mechanics and Simple Beam Theory (Kinloch et al. (1993); Carlsson et al. (1986)). In these equations, E_{11} is the longitudinal elastic modulus of the specimen, a is the crack length, and b, h and L are the width, the arm height and the half length of the specimen, respectively.

Table 4: Analytical equations of MMB test with $B = 0.0$.

MMB Test: $B = 0.0$ (pure mode I)	
Critical load	$P_c = \left(\dfrac{E_{11}b^2h^3G_{Ic}}{12a^2} \right)^{\frac{1}{2}}$
Compliance	$C = \dfrac{\Lambda_{LP}}{P} = \dfrac{8a^3}{bE_{11}h^3}$

Table 5: Analytical equations of ENF test $B = 1.0$ (pure mode II).

ENF Test: $B = 1.0$ (pure mode II)	
Critical load	$P_c = \left(\dfrac{16E_{11}b^2h^3G_{IIc}}{9a^2} \right)^{\frac{1}{2}}$
Compliance	$C = \dfrac{\Lambda_{LP}}{P} = \dfrac{3a^3+2L^3}{8bE_{11}h^3}$
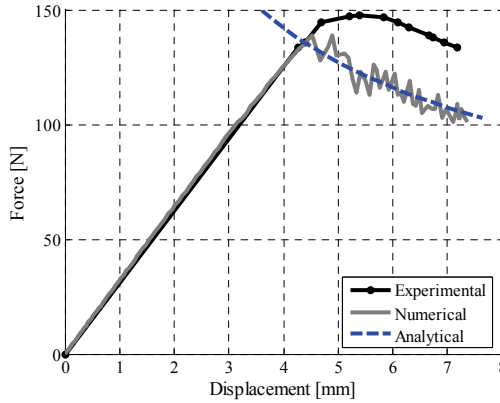
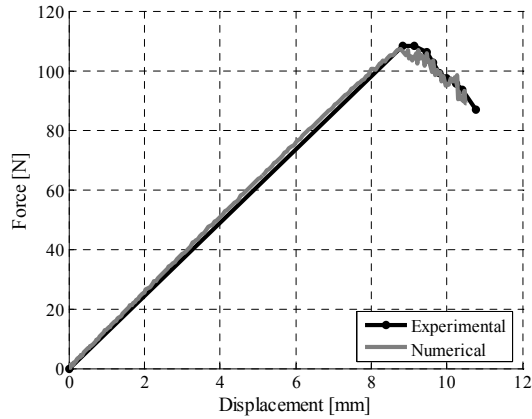Figure 10: Experimental and numerical force-displacement relation of the MMB test $B = 0.0$ (pure mode I).

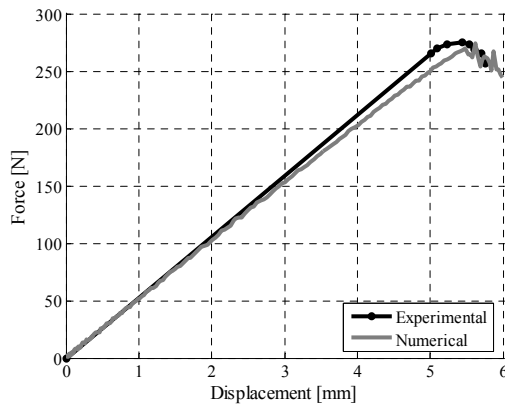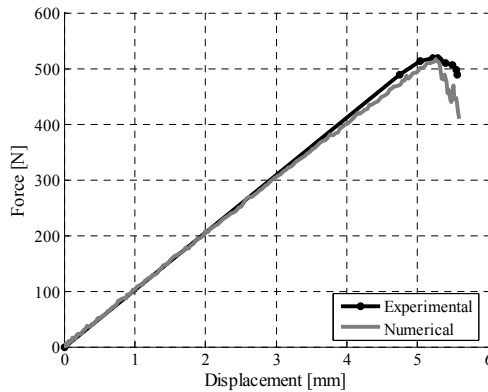Figure 11: Experimental and numerical force-displacement relation of the MMB test *B* = 0.2.

Figure 12: Experimental and numerical force-displacement relation of the MMB test *B* = 0.5.

6.2.5   Discussion

The charts obtained by numerical simulations of the proposed tests are in a good agreement with the experimental data. The predicted case of *B*= 0.0 (pure mode I) is the most far of the corresponding experimental chart. This difference is not due to limitations of the numerical simulations, but rather to the fact that the experimental fracture toughness used corresponds to the onset delamination and not

Figure 13: Experimental and numerical force-displacement relation of the MMB test $B = 0.8$.
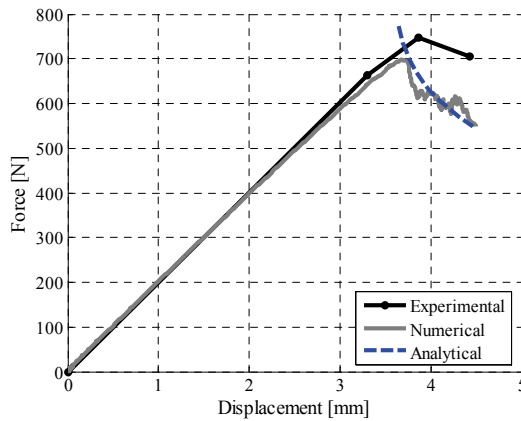

Figure 14: Experimental and numerical force-displacement relation of the ENF test (pure mode II).

to the propagation, which is normally larger than the onset fracture toughness. The analytical model which gives the relationship of the critical load and the displacement during propagation is plotted. The fracture toughness specified is $G_c = 0.969$ N/mm (see Tab. 3), and the numerical curve shows an excellent correlation with the descending part of the analytical load-displacement curve. On the other hand, the analytical model corresponding to the ENF test with a fracture toughness of $G_c = 1.719$ N/mm (see Tab. 3) is plotted in Fig. 14, which also shows a good agreement

between the analytical load-displacement curve and the numerical prediction.

Once the delamination is initiated, oscillations are observed in all predictions. However, the amplitude of these oscillations has been reduced by considering viscous algorithms and damping factors, by increasing the mesh refinement, and by reducing the loading velocity. Other possibility allowed for propagation tests which was not exposed here is to reduce the interface strength (Elmarakbi et al. (2006)).

In part, the oscillations which appear in a quasi-static explicit simulation may be a consequence of the constitutive equation shape. For implicit simulations, the shape of the constitutive equation does not affect to the results, whenever the fracture toughness is correctly accounted and the initial stiffness and maximum traction are reasonably consistent with the stiffness and strength of the material being modelled. However, in quasi-static explicit simulations, the shape has an important role for the stability simulation. The equation used has two discontinuities, one at initiation damage onset and other in the damage propagation. In some cases, stress waves appear at these points whose generate high frequency vibrations that break the cohesive element at the neighbourhood. Therefore, an attractive solution is to use constitutive equation shapes without discontinuities (Pinho et al. (2006)).

6.3   TCT tests

The simulations of quasi-static Transverse Crack Tension tests (TCT) of unidirectional zero degree layup specimens are analysed in this section.

6.3.1   Configuration of the TCT tests

The TCT specimens are manufactured by continuous fibre laminates with unidirectional stacking order whose central plies are cut prior to curing, as shown in Fig. 15. When these specimens are loaded by tension, delaminations develop under pure mode II. Such laminates are referred by $[0_m, \emptyset_n]_s$, where the slash indicates the cut plies.

The TCT specimens can be tested with or without pre-cracks previously induced. The specimens with pre-cracks are those undergoing a determined number of fatigue cycles at near-threshold loading for delamination growth. For no pre-cracked specimens, the gap between cut plies is a resin rich region which delaminates under pure mode I. Next, at certain load level, delamination starts at the corner point between cut and continuous plies along the fibre direction and quickly develops under pure mode II to certain length or full-scale. For pre-cracked specimens, this pre-delamination phase is not experimented since small initial interface cracks are previously created (Ye et al. (1990)). Consequently, the resulting critical load and fracture toughness are more representative in these specimens than for no pre-

cracked specimens.

The TCT test is then an alternative to the ENF test (König et al. (1997)). It is assumed that in the TCT test there is less sliding friction between the delaminated plies than in the ENF test. A second advantage concerns compliance calibration for data reduction. The compliance of the TCT specimen is less sensitive to the error in crack length measurement, because the compliance is related linearly to the crack length a (see Eq. 82), whereas for the ENF specimen the compliance is related to a^3 (see Tab. 5).

$$C = \frac{\Lambda}{P} = \frac{L(t - t_c) + 2at_c}{bt(t - t_c)E_{11}} \tag{82}$$

E_{11} is the longitudinal elastic modulus of the specimen, a is the length of one crack, and t_c is the whole thickness of cut central plies. The geometrical variables L, b and t are the length, width, and total thickness of the specimen, respectively (see Fig. 15).
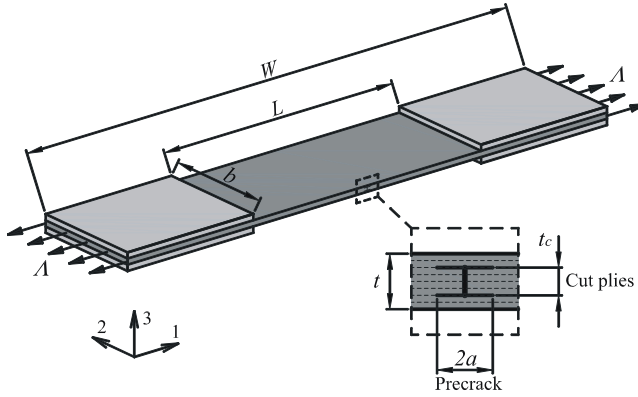

Figure 15: TCT specimen.

From the evaluation of the compliance C and the delamination length a (see Eq. 82), the fracture toughness G_{IIc} can be derived for a constant specimen width b as:

$$G_{IIc} = \frac{1}{4} \frac{t_c P_c^2}{b^2 E_{11} t(t - t_c)} \tag{83}$$

The factor $1/4$ is introduced because there are four crack tips. Eq. 83 shows that G_{IIc} can be obtained by determining solely the critical load P_c.

Only no pre-cracked specimens are simulated. The laminates considered are: $[0_2, /\ 0_4]_s$, $[0_4, \emptyset_4]_s$ and $[0_4, \emptyset_8]_s$. The numerical results obtained are basically the critical

load P_c for delamination propagation, and are compared with experimental values performed by Ye et al. (1990).

6.3.2   Sizes and types of the elements

Two delamination planes are modelled in the TCT specimens, as shown in Fig. 16. One corresponds to the interface of the cut central plies which delaminates under pure mode I, and is modelled by using zero-thickness type elements with four integration points of the Abaqus element library (i.e. COH3D8). The other delamination plane corresponds to the interface between cut and continuous plies along the fibre direction which delaminates under pure mode II. In this case, the interface is modelled by using non-zero-thickness type elements with reduced integration (i.e. C3D8R). The thickness defined for this interface is 0.01 mm, which is much smaller than the value obtained by means of Eq. 73. The in-plane length of these elements at the crack propagation direction is determined by means of Eq. 74 and 75. If three elements are desired to be along the cohesive length, the maximum in-plane length is of 0.37 mm. The length finally used is 0.33 mm.
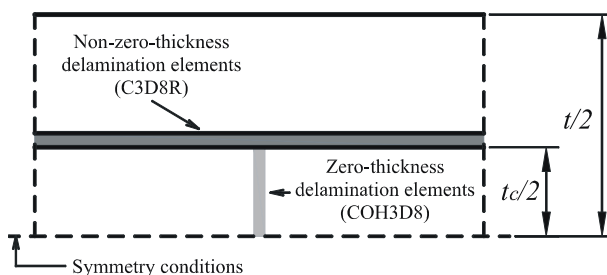

Figure 16: Detail of the location of the cohesive elements.

The specimen width is meshed with five elements, and each ply thickness with two elements. The composite material is modelled by using also C3D8R elements. Only half thickness of the specimen is modelled by defining symmetric boundary conditions.

6.3.3   Materials and specimen dimensions

The composite material used is an epoxy matrix-based reinforced by unidirectional carbon fibres (T300/914C). The properties are extracted from Ye et al. (1990) and set in Tab. 6.

The material properties defined to the interface elements located between cut and continue plies are shown in Tab. 7, and are selected by considering that these

elements represent a resin-rich layer. The fracture toughness G_{IIc} is obtained by testing pre-cracked TCT specimens (Ye et al. (1990)). For zero-thickness cohesive elements the properties are equal than those set in Tab. 7 except the elastic modulus (i.e. penalty stiffness) which is set 1e6, and in order to obtain the same penalty stiffness for all propagation modes the Poisson modulus is set equal to -0.5.

Table 6: T300/914C properties.

E_{11} (MPa)	$E_{22} = E_{33}$ (MPa)	$G_{12} = G_{13}$ (MPa)	G_{23} (MPa)	$\nu_{12} = \nu_{13}$	ν_{23}	ρ (t/mm^3)
129000	9256 MPa	5000 MPa	3306 MPa	0.28	0.4	1600e-12

Table 7: Interface properties.

E_m (MPa)	ν_m	ρ_m (t/mm^3)	τ_3^o (MPa)	τ_1^o (MPa)	G_{Ic} (N/mm)	G_{IIc} (N/mm)
9256	0.3	1600e-12	50	59	0.17	0.467

The parameter η is approached to 1.47, which is obtained by means of least-square fit of mixed-mode fracture toughnesses obtained in MMB tests (König et al. (1997)).

The dimensions of the specimens are: 140 mm long (L), 20 mm wide (b), and the ply thickness is approximately 0.125 mm. The total length of the specimens is 380 mm (W).

6.3.4   Results and discussion

The load-displacement relations obtained in the finite element simulations of each TCT specimen are plotted in Fig. 17. These Figures show a peak load which corresponds to the point where the interface of the cut central plies is completely damaged. Next, stationary load values appear after the drop of the peak loads (i.e. after the pre-delamination phase). These stationary loads are the critical loads for pure mode II delamination of the interface between cut and continue plies. By means of Eq. 83 and the numerical critical loads obtained, the fracture toughness G_{IIc} can be predicted. The results are set in Tab. 8 and show a good agreement with the value defined in the model: G_{IIc} = 0.467 N/mm. On the other hand, a comparison of the results shown in Tab. 8 indicates good correlation between the predicted peak loads and the corresponding experimental values.
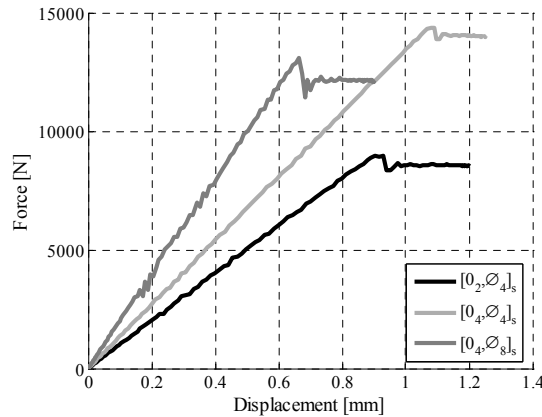
Figure 17: Numerical load-displacement relations for the TCT specimens.

Table 8: Experimental and numerical results.

Laminate	Experimental P_{peak} (N)	Numerical P_{peak} (N)	Numerical P_c (N)	Numerical G_{IIc} (N/mm)
$[0_2, \emptyset_4]_s$	8500	8963	8600	0.478
$[0_4, \emptyset_4]_s$	15219	14380	14200	0.488
$[0_4, \emptyset_8]_s$	14321	13080	12100	0.473

7 Conclusions

The formulation and implementation of a thermodynamically consistent damage model for the simulation of progressive delamination in composite materials under variable mixed-mode ratio by using an explicit finite element code was presented. The model was formulated in the context of Damage Mechanics, and implemented by means of a user-written material subroutine. The user material can be defined on sets of elements that represent the possible location for delamination. The elements can be selected to have zero-thickness (surface elements) or non-zero-thickness (continuum elements).

The model was used to simulate the initiation and propagation of delamination in fracture toughness tests (MMB, ENF and TCT) under quasi-static loading conditions. The examples analyzed are in good agreement with the test results, and they indicate that the proposed formulation can predict the delamination process of composite structures that exhibit progressive delamination. It should be noted that some numerical predictions have showed some stability problems or oscilla-

tions which have been reduced significantly by considering viscous algorithms and damping factors, by increasing the mesh refinement, and by reducing the loading velocity during the crack propagation process. However, these oscillations may be reduced even more by modifying the shape of the constitutive equation to one without discontinuity points.

To make use of the damage model implemented and of the explicit finite element code, the next step is to simulate low-velocity impacts of foreign objects on monolithic laminated composite plates, where the delamination generally propagates under variable mixed-mode conditions. In these analyses, the study of the shape and extension of the delamination at interfaces between mismatch orientation layers is of great interest since the delamination can reduce dramatically the damage tolerance of the structure. In order to carry out an accurately prediction, an intralaminar damage model must be added in these analyses (such as the model developed in Maimí et al. (2007a) and (2007b)), since impact loading conditions creates intralaminar damage mechanisms which interact with the delamination failure mode.

References

ABAQUS version 6.8 (2008): ABAQUS User's Manual. *SIMULIA World Headquarters*, 166 Valley Street, Providence, RI 02909, USA.

Alfano, G.; Crisfield, M.A. (2001): Finite element interface models for the delamination analysis of laminated composites: mechanical and computational issues. In: *International Journal of Numerical Methods in Engineering*, vol. 77, pp. 111-170.

Allix, O.; Ladeveze, P.; Corigliano, A. (1995): Damage analysis of interlaminar fracture specimens. In: *Composite Structures*, vol. 31, pp. 66-74.

Aymerich, F.; Dore, F.; Priolo, P. (2008): Prediction of impact-induced delamination in cross-ply composite laminates using cohesive interface elements. In: *Composites Science and Technology*, vol. 68, pp. 2383-2390.

Babuska, I.; Melenk, J.M. (1997): The partition of unity method. In: *International Journal of Numerical Methods in Engineering*, vol. 40, pp. 727-758.

Barenblatt, G.I. (1962): The mathematical theory of equilibrium cracks in brittle fracture. In: *Advanced Applied Mechanics*, vol. 7, pp. 55–129.

Bažant, Z.P.; Oh, B.H. (1983): Crack band theory for fracture of concrete. In: *Materials and Structures*, vol. 16, pp. 155-177.

Belytschko, T.; Moës, N.; Usui, S.; Parimi, C. (2001): Arbitrary discontinuities in finite elements. In: *International Journal for Numerical methods in Engineering*, vol. 50, pp. 993-1013.

Benzeggagh, M.L.; Kenane, M. (1996): Measurement of Mixed-Mode delamination Fracture Toughness of Unidirectional Glass/Epoxy Composites with Mixed-Mode Bending Apparatus. In: *Composites Science and Technology,* Elsevier, pp. 439-449.

Bergan, P.G.; Mollestad, E. (1985): An automatic time-stepping algorithm for dynamic problems. In: *Computer Methods in Applied Mechanics and Engineering*, vol. 49, pp. 299-318.

Camanho, P.P.; Dávila C.G.; De Moura, M. (2003): Numerical simulation of mixed-mode progressive delamination in composite materials. In: *Journal of Composite Materials,* Sage publications, vol. 37, num. 16, pp. 1415-1438.

Carlsson, L.A.; Gillespie, J.W.; Pipes, R.B. (1986): On the analysis and design of the end notched flexure (ENF) specimen for mode II testing. In: *Journal of Composite Materials*, vol. 20, pp. 594-604.

Corigliano, A.; Allix, O. (2000): Some aspects of interlaminar degradation in composites. In: *Computer Methods in Applied Mechanics and Engineering*, vol. 185, pp. 203-224.

Crews, J.H.; Reeders, J.R. (1998): Mixed-mode bending method apparatus for delamination testing. In: *NASA TM 100662.*

De Borst, R. (2003): Numerical aspects of cohesive-zone models. In: *Engineering Fracture Mechanics*, vol. 70, pp. 1743-1757.

De Borst, R.; Remmers, J.J.C.; Needleman, A. (2006): Mesh-independent discrete numerical representations of cohesive-zone models. In: *Engineering Fracture Mechanics*, vol. 73, pp. 160-177.

Dugdale, D.S. (1960): Yielding of steel sheets containing slits. In: *Journal of Mechanics and Physics of Solids*, vol. 8, issue 2, pp. 100-104.

Elmarakbi, A.M.; Hu, N.; Fukunaga, H. (2006): Implementation of new adaptive cohesive elements for the simulations of delamination in composite materials in LS-DYNA. In: *Material III – Foams / Composites*, LS-DYNA Anwenderforum, UIm.

Griffith, A.A. (1921): The phenomena of rupture and flow in solids. In: *Philosophical Transactions of the Royal Society of London*, vol. 221, pp. 163-198.

Hashin, Z. (1980): Failure criteria for unidirectional fiber composites. In: *Journal*

of Applied Mechanics, pp. 329-334.

Hellen, T.K. (1975): On the method of the virtual crack extension. In: *International Journal of Numerical Methods in Engineering*, vol. 9, pp. 187-207.

Hillerborg, A.; Modeer, M.; Petersson, P.E. (1976): Analysis of crack formation and crack growth in concrete by means of fracture mechanics and finite elements. In: *Cement Concrete Research*, vol. 6, pp. 773-782.

Iannucci, L. (2006): Dynamic delamination modelling using interface elements. In: *Computers and Structures*, vol. 84, pp. 1029-1048.

Irwin, G.R. (1957): Analysis of stresses and strains near the end of a crack transversing a plate. In: *Journal of Applied Mechanics*, vol. 24, pp. 361–366.

Jansson, N.E.; Larsson, R. (2003): Rotational interface formulation for delamination analysis of composite laminates. In: *Computers and Structures*, vol. 81, pp. 2705-2716.

Kinloch, A.J.; Wang, Y.; Williams, J.G.; Yayla, P. (1993): The mixed-mode delamination of fiber composite-materials. In: *Composites Science and Technology*, vol. 47, pp. 225-237.

König, M.; Krüger, R.; Kussmaul, K.; Alberti, M. v.; Gädke, M. (1997): Characterizing static and fatigue interlaminar fracture behaviour of a first generation graphite/epoxy composite. In: *Composite Materials: Testing and Design¸* ASTM STP 1242, vol. 13, pp. 60-81.

Krueger, R. (2002): The virtual crack closure technique: history, approach and applications. In: *NASA/CR-2002-211628*.

Maimí, P.; Camanho, P.P.; Mayugo, J.A.; Dávila, C.G. (2007a): A continuum damage model for composite laminates: Part I – Constitutive model. In: *Mechanics of Materials*, vol. 39, issue 10, pp. 897-908.

Maimí, P.; Camanho, P.P.; Mayugo, J.A.; Dávila, C.G. (2007b): A continuum damage model for composite laminates: Part II – Computational implementation and validation. In: *Mechanics of Materials*, vol. 39, issue 10, pp. 909-919.

Martha, L.; Wawrzynek, P.A.; Ingraffea A.R. (1993): Arbitrary crack propagation using solid modelling. In: *Engineering with Computers*, vol. 9, pp. 63-82.

Mazars, J. (1982): Mechanical Damage and Fracture of Concrete Structures. In: *Advances in Fracture Research*. Ed. Pergamon Press, Oxford.

Mi, U.; Crisfield, M.A.; Davies, G.A.O. (1998): Progressive delamination using interface elements. In: *Journal of Composite Materials*, vol. 32, pp. 1246-1272.

National Research Concil of the National Academies (2006): Going to extremes, meeting the emerging demand for durable polymer matrix composites. In: *The*

National Academies Press, Washington, DC, USA.

Oliver, J. (2000): On the discrete constitutive models induced by strong discontinuity kinematics and continuum constitutive equations. In: *International Journal of Solids and Structures*, vol. 37, pp. 7207-7229.

Oliver, J.; Cervera, M.; Oller, S.; Lubliner, J. (1990): Isotropic damage models and smeared crack analysis of concrete. In: *Second International Conference on Computer Aided Analysis and Design of Concrete Structures (Austria)*, vol. 2, pp. 945-958.

Ortiz, M.; Pandolfi A. (1999): Finite-deformation irreversible cohesive elements for three-dimensional crack-propagation analysis. In: *International Journal for Numerical Methods in Engineering*, vol. 44, pp. 1267-1282.

Pagano, N.J.; Pipes, R.B. (1973): Some observations on the interlaminar strength of composite laminates. In: *International Journal of Mechanical Science*, vol. 15, pp. 679-688.

Papadrakakis, M. (1981): A method for the automatic evaluation of the dynamic relaxation parameters. In: *Computer Methods in Applied Mechanics and Engineering*, vol. 25, pp. 35-48.

Parks, D.M. (1974): A stiffness derivative finite element technique for determination of crack tip stress intensity factors. In: *International Journal of Fracture*, vol. 10, pp. 487-502.

Pinho, S.T.; Iannucci, L.; Robinson, P. (2006): Formulation and implementation of decohesion elements in an explicit finite element code. In: *Composites Part A: Applied Science and Manufacturing*, Elsevier, vol. 37, issue 5, pp. 778-789.

Prinz, R.; Cao, L. (1989): Analysis of strain-energy-release rates for unidirectional graphite/epoxy laminates with separated central plies under fatigue loading. In: *Proceedings of Seventh International Conference on Composite Materials: ICCM-VII (Beijing, China)*.

Raju, I.S. (1987): Calculation of strain-energy release rates with higher order and singular finite elements. In: *Engineering Fracture Mechanics*, vol. 38, pp. 251-274.

Reeder, J.R.; Crews, J.H. (1990): Mixed-mode bending method for delamination testing. In: *AIAA J.*, vol. 28, pp. 1270-1276.

Reeder, J.R.; Crews, J.H. (1991): Non-linear analysis and redesign of the mixed-mode bending delamination test. In: *NASA TM 102777*.

Remmers, J.J.C.; De Borst, R.; Needleman, A. (2003): A cohesive segments method for the simulation of crack growth. In: *Computational Mechanics*, vol. 31, pp. 69-77.

Rice, J.R. (1968): A path independent integral and the approximate analysis of strain concentration by notches and cracks. In: *ASME Journal of Applied Mechanics*, vol. 35, pp. 379-386.

Rice, J.R. (1980): The mechanics of earthquake rupture. In: *Physics of the Earth's Interior (Proc. International School of Physics "Enrico Fermi", Course 78, 1979; ed. A.M. DZIEWONSKI and E. BOSCHI),* Italian Physical Society and North-Holland Publ. Co.

Rybicki, E.F.; Kanninen, M.F. (1977): A finite element calculation of stress intensity factors by a modified crack closure integral. In: *Engineering Fracture Mechanics*, vol. 9, pp. 31-938.

Sauvé, R.G.; Metzger, D.R. (1995): Advances in dynamic relaxation techniques for nonlinear finite element analysis. In: *The American Society of Mechanical Engineers*, vol. 117, pp. 170-176.

Schellekens, J.C.J.; De Borst, R. (1993): A nonlinear finite-element approach for the analysis of mode-I free edge delamination in composites. In: *International Journal of Solids and Structures*, vol. 30, num. 9, pp. 1239-1253.

Simo, J.C.; Ju, J.W. (1987): Strain- and stress- based continuum damage model I. Formulation. In: *International Journal Solids Structures*, vol. 23, issue 7, pp. 821-840.

Simo, J.C.; Rifai, M.S. (1990): A class of mixed assumed strain methods and the method of incompatible modes. In: *International Journal of Numerical Methods in Engineering*, vol. 29, pp. 1595-1638.

Turon, A.; Camanho, P.P.; Costa J.; Dávila, C.G. (2006): A damage model for the simulation of delamination in advanced composites under variable-mode loading. In: *Mechanics of Materials*, Elsevier, vol. 38, issue 11, pp. 1072-1089.

Turon, A.; Dávila, C.G.; Camanho, P.P.; Costa J. (2007): An engineering solution for mesh size effects in the simulation of delamination using cohesive zone models. In: *Engineering Fracture Mechanics*, vol. 74, pp. 1665-1682.

Xu, X.P.; Needleman, A. (1994): Numerical simulations of fast crack growth in brittle solids. In: *Journal of Mechanics and Physics of Solids*, vol. 42, pp. 1397-1434.

Yang, Q.; Cox, B. (2005): Cohesive models for damage evolution in laminated composites. In: *International Journal of Fracture*, vol. 133, pp. 107-137.

Ye, L. (1988): Role of matrix resin in delamination onset and growth in composite laminates. In: *Composites Science and Technology*, vol. 33, pp. 257-277.

Ye, L.; Prinz, R.; Klose, R. (1990): Characterization of interlaminar shear fracture toughness and delamination fatigue growth of composite materials using TCT

specimen. In: *Report IB 131-90/15, DLR, Institute for Structural Mechanics*.

Zhang, Y.; Zhu, P.; Lai, X. (2006): Finite element analysis of low-velocity impact damage in composite laminated plates. In: *Materials and Design*, vol. 27, pp. 513-519.

Zou, Z.; Reid, S.R.; Li, S.; Soden, P.D. (2001): Mode separation of energy release rate for delamination in composite laminates using sub-laminates. In: *International Journal of Solids and Structures*, vol. 38, pp. 2597-2613.